Molecular basis of sphingosine-1-phosphate transport by MFSD2B provides insights for selective inhibitor screening

Bin Pang[1,2] †, Leiye Yu[1,3] †, Bing Gan[1] †, Zhaoyang Qin[1], Weidi Wang[1], Rujuan Ti[4], Ruiping He[5], Jinxin Wang[6], Yufei Han[7], Haizhan Jiao[8], Hongli Hu[8], Lizhe Zhu[4], Li Chen[5], Tian Xie[9] *, Ruobing Ren[1,2] *

[1] Shanghai Key Laboratory of Metabolic Remodeling and Health, Institute of Metabolism and Integrative Biology, Fudan University, Shanghai, China

[2] Shanghai Xuhui Central Hospital, Zhongshan-Xuhui Hospital, Fudan University, Shanghai, China

[3] Department of Otorhinolaryngology Head and Neck Surgery, Shanghai Sixth People's Hospital Affiliated to Shanghai Jiao Tong University School of Medicine, Shanghai, China

[4] Warshel Institute of Computational Biology, School of Life and Health Sciences, the Chinese University of Hong Kong, Shenzhen, Guangdong 518172, China

[5] Shanghai Key Laboratory of Metabolic Remodeling and Health, Institute of Metabolism and Integrative Biology, Obstetrics and Gynecology Hospital, Fudan University, Shanghai 200438, China

[6] Department of Phytochemistry, School of Pharmacy, Second Military Medical University (Naval Medical University), Shanghai, 200433, China.

[7] Laboratory of Biomolecular Research, Paul Scherrer Institute, Villigen, Switzerland

[8] Kobilka Institute of Innovative Drug Discovery, School of Life and Health Sciences, the Chinese University of Hong Kong, Shenzhen, Guangdong 518172, China

[9] MOE Key Laboratory of Geriatric Diseases and Immunology, Biomedical Basic Research Center of Jiangsu, Institute of Molecular Enzymology, School of Life Sciences, Suzhou Medical College of Soochow University, Suzhou, Jiangsu, 215123, China

* To whom correspondence should be addressed. Email: renruobing@fudan.edu.cn

† These authors contributed equally

Abstract

Sphingosine-1-phosphate (S1P) is a bioactive sphingolipid that regulates immune cell trafficking, vascular homeostasis, and platelet function. MFSD2B, a major facilitator superfamily transporter, maintains plasma S1P levels by exporting S1P from erythrocytes and platelets, yet the molecular basis of S1P recognition and transport by MFSD2B remains unclear. Here, we report a 3.65 Å cryo-EM structure of *Sus scrofa* MFSD2B captured in an outward-facing conformation. Together with AlphaFold3-based modeling, molecular docking and dynamics simulations, and mutagenesis-based transport assays, our results identify a distributed S1P-recognition pathway required for MFSD2B transport. Comparative analyses show that MFSD2B preserves the lipid-transport features of MFSD2A but lacks LPC-recognition and Na^+-coupling sites. Despite sharing S1P transport activity, MFSD2B and SPNS2 recognize the phosphate headgroup of S1P through distinct pocket architectures. Current S1P-mimic SPNS2 inhibitors cross-react with MFSD2B, highlighting the need for scaffold-divergent inhibitors with improved transporter selectivity. We establish a transporter-receptor conjugated screening (TRCS) system to enable efficient and cost-effective inhibitor screening. Together, our findings provide a structural framework for S1P transport by MFSD2B and may facilitate the discovery of selective lipid transporter inhibitors.

Introduction

Sphingosine-1-phosphate (S1P) is a bioactive sphingolipid that regulates diverse physiological processes, including lymphocyte egress, endothelial barrier integrity, angiogenesis, and platelet activation [1]. S1P signaling relies on steep concentration gradients between the circulation and peripheral tissues: S1P is maintained at relatively high levels in blood and lymph but remains much lower in most tissues, thereby directing the trafficking of cells expressing S1P receptors [2]. Because S1P is amphipathic and does not freely traverse lipid bilayers, dedicated membrane transporters are required for its export into the extracellular space.

Among the transporters that sustain extracellular S1P, SPNS2 and MFSD2B make particularly important but distinct contributions [3, 4]. SPNS2 is expressed predominantly in vascular and lymphatic endothelial cells, where it mediates S1P secretion into blood and lymph and supports immune cell trafficking and vascular homeostasis [5]. By contrast, MFSD2B is highly expressed in erythrocytes and platelets and serves as the principal S1P transporter in these hematopoietic cells [4]. Erythrocytes constitute a major source of circulating S1P under basal conditions, whereas platelets provide an additional activation-dependent source [6]. Consistent with this functional partitioning, loss of SPNS2 primarily disrupts endothelial and lymphatic S1P export and lymphocyte trafficking, whereas loss of MFSD2B markedly reduces plasma S1P and alters S1P

handling in blood cells [4, 6]. The more severe impairment caused by combined transporter deficiency further indicates that SPNS2 and MFSD2B act in complementary rather than redundant roles in systemic S1P homeostasis [4, 6], highlighting the importance of transporter selectivity when targeting S1P export pharmacologically.

MFSD2B belongs to the major facilitator superfamily (MFS), whose members typically comprise 12 transmembrane helices arranged as two pseudo-symmetric six-helix bundles and operate through an alternating-access mechanism[7]. Within the lysolipid-transporting branch of this superfamily, MFSD2B is most closely related to MFSD2A, a sodium-coupled lysophosphatidylcholine (LPC) transporter that mediates LPC uptake at the blood–brain barrier [8]. Despite this close relationship, MFSD2B transports S1P rather than lysophospholipids and therefore shares substrate preference with SPNS2 rather than MFSD2A. This convergence in S1P specificity despite limited sequence similarity within a shared MFS scaffold raises fundamental questions about the structural determinants of S1P recognition and selectivity. Recent structural studies of SPNS2 and MFSD2A have clarified important principles of S1P and LPC transport, respectively [9, 10]. However, the molecular basis of S1P recognition by MFSD2B, the structural features that distinguish it from MFSD2A and SPNS2, and the implications of these differences for selective inhibitor development remain unresolved.

Here, we report a 3.65 Å cryo-EM structure of *Sus scrofa* MFSD2B

(SsMFSD2B) captured in an apo, outward-facing conformation. SsMFSD2B shares 85% sequence identity with *Homo sapiens* MFSD2B (HsMFSD2B), supporting its relevance as a structural model for the human transporter. By integrating this structure with AlphaFold3-predicted inward-facing models, molecular docking, molecular dynamics (MD) simulations, and structure-guided mutagenesis, we identify key determinants involved in S1P recognition and transport. Comparisons with MFSD2A reveal structural features underlying the divergence in substrate specificity and energy-coupling mechanisms between these closely related transporters. Comparisons with SPNS2 further show that, despite sharing S1P transport activity, MFSD2B recognizes S1P through a distinct pocket architecture. Although reported S1P-mimic inhibitors of SPNS2 cross-react with MFSD2B, the non-conserved pocket features of these two transporters suggest opportunities to conduct compound screening for developing selective inhibitors with novel scaffolds to reduced cross-activity. To support such efforts, we establish a transporter-receptor conjugated screening (TRCS) system that replaces low-throughput mass spectrometry (MS)-based S1P quantification with a scalable and cost-effective bioluminescence resonance energy transfer (BRET)-based readout for inhibitor discovery. Together, our study provides a structural framework for S1P recognition and transport by MFSD2B and guides the discovery of selective lipid transporter inhibitors.

Results

Functional validation and cryo-EM structure of SsMFSD2B

To investigate the structural basis of S1P transport by MFSD2B, we screened eight MFSD2B orthologues and identified *Sus scrofa* MFSD2B (SsMFSD2B) as the most stable and highly expressed candidate for structural analysis. SsMFSD2B shares 85% sequence identity with human MFSD2B (HsMFSD2B) (Supplementary Fig. S1). To assess whether SsMFSD2B is functionally representative of HsMFSD2B, we expressed SsMFSD2B, HsMFSD2B, and HsSPNS2 in HEK293T cells and quantified S1P export by mass spectrometry. All three transporters promoted significantly greater S1P export than the empty-vector control, and SsMFSD2B displayed activity comparable to that of HsMFSD2B (Fig. 1A). Immunofluorescence microscopy confirmed plasma membrane localization for all constructs (Fig. 1B). Together, these data establish SsMFSD2B as a functional homolog of HsMFSD2B and support its use for structural and functional analysis.

We next determined the structure of SsMFSD2B by single-particle cryo-EM, which yielded a density map of apo SsMFSD2B at an overall resolution of 3.65 Å (Fig. 1C, Supplementary Fig. S2A-F, and Table S1), enabling model building for residues 31-205, 221-255, and 264-476 (Supplementary Fig. S2G). SsMFSD2B adopts the canonical MFS architecture, comprising two pseudo-symmetric six-helix bundles that form the N-terminal domain (NTD; TM1-TM6) and C-terminal domain

(CTD; TM7-TM12), connected by a flexible intracellular loop (Fig. 1D). The structure was captured in an outward-facing conformation, with an open extracellular vestibule and a sealed cytoplasmic side. A central amphipathic cavity extends from the extracellular opening toward the membrane midplane between NTD and CTD. Electrostatic potential surface analysis revealed a heterogeneous charge distribution within the bottom of cavity, with negatively and positively charged patches interspersed among hydrophobic regions (Fig. 1E), consistent with the accommodation of an amphipathic lipid substrate. Although additional density was observed near the extracellular side of the central cavity, adjacent to TM7–TM8, TM11, and ECL6, it could not be confidently assigned to S1P (Supplementary Fig. S2H).

Putative S1P recognition sites in MFSD2B

To identify potential substrate-binding sites in MFSD2B, we first docked S1P into the central cavity of the outward-facing SsMFSD2B structure using AutoDock Vina [18]. In the top-ranked docking pose, the hydrophobic tail of S1P wraps around TM10-TM11 in the CTD, whereas the polar headgroup is positioned within a polar sub-pocket formed mainly by residues from the NTD, including R181, E185, Q52, and Q157 (Fig. 2A and B). To explore substrate recognition in an alternative conformational state, we next used a locally installed version of AlphaFold3 to predict S1P-bound models of SsMFSD2B. The top-ranked

models consistently adopted an inward-facing conformation, with the alkyl tail of S1P inserted into a narrow hydrophobic pocket in the CTD and the polar headgroup positioned within a sub-pocket of the central cavity at the NTD-CTD interface (Fig. 2C and Supplementary Fig. S3A). In this predicted inward-facing state, the hydrophobic tail of S1P is surrounded mainly by residues from TM7, TM8, and TM10, whereas the phosphate group is positioned to interact with the positively charged residue K85. Additional polar residues, including Q52, Q295, Q298, and S55, further stabilize the local conformation around the S1P headgroup (Fig. 2D). The arrangement of S1P in both states suggests that the amphipathic S1P molecule is accommodated by a composite pocket in which the hydrophobic tail is stabilized by the CTD and the polar headgroup is recognized by charged and polar residues from the NTD.

Given the high sequence identity between SsMFSD2B and HsMFSD2B, as well as the conservation of the putative substrate-binding residues (Supplementary Fig. S3A-C), we next evaluated the functional roles of key pocket residues in HsMFSD2B by site-directed mutagenesis. In the outward-facing conformation, we targeted polar residues surrounding the S1P headgroup for mutational analysis. In cell-based transport assays, alanine substitution of R184 and E188 on TM5 correspond to SsMFSD2B R181 and E185, which interact with the S1P headgroup in the outward-facing docking model. Alanine substitution of either R184 or E188 markedly impaired S1P transport activity, whereas the R184A/E188A

double mutant nearly abolished S1P transport (Fig. 2E). In contrast, alanine substitution of M185 on TM5 (corresponding to SsMFSD2B M182) and W390 on TM10 (corresponding to SsMFSD2B W387) had no effects on S1P export, suggesting that these residues play a limited or indirect role in substrate recognition despite their proximity to the predicted binding pocket (Fig. 2E). In the inward-facing conformation, alanine substitution of Q298 and Q301 on TM7 (corresponding to SsMFSD2B Q295 and Q298 respectively) significantly impaired S1P transport, while L304A on TM7 (corresponding to SsMFSD2B L301) caused only a modest reduction. These results support a critical role for the putative polar sub-pocket in S1P recognition and transport by MFSD2B.

MFSD2B diverges from MFSD2A in LPC recognition and Na^+ coupling

MFSD2A is the closest homolog of MFSD2B and functions as a sodium-coupled lysophosphatidylcholine (LPC) transporter at the blood-brain barrier, where it mediates LPC uptake essential for brain DHA homeostasis. HsMFSD2B shares 38.8% sequence identity and 54.1% similarity with *Homo sapiens* MFSD2A (HsMFSD2A) over 462 aligned residues (Supplementary Fig. S4). However, MFSD2B has been reported to lack LPC transport activity [4]. To elucidate the structural basis for this functional divergence, we compared our AlphaFold3-predicted inward-facing SsMFSD2B model with experimentally determined LPC-bound

inward-facing structures of *Danio rerio* MFSD2A (DrMFSD2A; PDB IDs: 8D2U and 8D2V) [9] (Fig. 3A). Structural superposition showed that the overall MFS folds of SsMFSD2B and DrMFSD2A are highly conserved, with RMSD values of 2.454 Å and 2.683 Å over 439 and 441 Cα atoms, respectively. In these models, the hydrophobic tail of S1P in SsMFSD2B and the acyl chains of LPC in DrMFSD2A occupy a similar CTD-associated hydrophobic pocket (Fig. 3A, left inset). By contrast, the LPC headgroup-binding region is substantially remodeled. Several residues implicated in LPC recognition in DrMFSD2A, including Y50, D87, Q152, H156, and S160, correspond to N51, G88, A153, Q157, and T161 in SsMFSD2B, respectively (Fig. 3A, right inset). Because alanine substitution of D87 in DrMFSD2A abolishes LPC transport, whereas mutation of Q152 reduces transport activity [9], the lack of conservation of these LPC-recognition residues in MFSD2B provides a structural explanation for its inability to transport LPC.

We next compared our experimentally determined outward-facing SsMFSD2B structure with the outward-facing mouse MFSD2A structure (MsMFSD2A; PDB ID: 7N98) [11] (Fig. 3B). The two structures superimpose with an RMSD of 2.396 Å over 401 Cα atoms, further supporting conservation of the overall MFS scaffold. However, marked differences are observed at the canonical Na^+-binding site. In MFSD2A, Na^+ coordination is mediated by D92, T95, D96, T163, and K433. In SsMFSD2B, two key acidic and polar residues, D92 and T95, are replaced

by G88 and A91, respectively. These substitutions remove side chains that contribute to Na^+ coordination in MFSD2A and disrupt the chemical environment required for stable Na^+ binding. Consistent with this structural divergence, all-atom MD simulations with Na^+ placed at the putative binding site showed rapid ion dissociation across three independent 100-ns trajectories, with Na^+ only transiently sampling the pocket before diffusing away (Supplementary Video S1).

We further tested ion dependence using S1P export assays. Replacement of extracellular Na^+ with either K^+ or the impermeant cation N-methyl-D-glucamine (NMDG) had no significant effect on SsMFSD2B-mediated S1P export (Fig. 3C), indicating that S1P transport by SsMFSD2B is independent of extracellular Na^+. Together, these structural comparisons, MD simulations, and functional analysis indicate that MFSD2B preserves the lipid-translocation scaffold of MFSD2A but lacks the LPC headgroup-recognition and Na^+-coordination features of MFSD2A.

MFSD2B and SPNS2 recognize S1P through distinct pocket architectures

MFSD2B and SPNS2 both belong to the MFS superfamily and function as S1P transporters that mediate S1P export from the cytoplasm to the extracellular space. Despite this functional convergence, HsMFSD2B and SsMFSD2B share very low sequence identity with HsSPNS2, 14.3% and 15.9%, respectively. This pronounced sequence divergence prompted us to

examine how these transporters achieve S1P recognition within a shared MFS scaffold.

Firstly, we compared our experimentally determined outward-facing SsMFSD2B structure and predicted inward-facing SsMFSD2B model with reported HsSPNS2 structures in outward- and inward-facing conformations. Typically, the NTD and CTD of MFS transporters are two-fold pseudo symmetric. After superimposing the NTDs of the two outward-facing structures of SsMFSD2B and HsSPNS2, with an overall Cα RMSD of 5.983Å over 145 aligned residues, we observed a pronounced rigid-body displacement of the CTDs, particularly involving TM7, TM11, and TM12 (Fig. 4A). A similar NTD-based alignment of the inward-facing structures, with an overall Cα RMSD of 9.614 Å over 78 aligned residues, also revealed substantial displacement of CTDs (Fig. 4B). Despite these global differences, the hydrophobic tail of S1P in SsMFSD2B occupies a CTD-associated pocket that is spatially analogous to the S1P-binding pocket observed in HsSPNS2 (Fig. 4C, inset). In both transporters, the alkyl tail of S1P is accommodated within a hydrophobic groove, suggesting a shared tail-anchoring principle. Previous studies of HsSPNS2 identified three positively charged residues, R227, R119, and R200, that are located along the transport path and required for efficient S1P transport, possibly by recognizing the phosphate group and facilitating the flipping of S1P across the membrane. Similarly, in MFSD2B, R174, R181, and K85 are positioned along the putative S1P transport path (Fig.

4C, inset). However, these charged residues are not conserved in their spatial arrangement between MFSD2B and SPNS2, indicating that the two transporters use distinct charged-residue architectures for phosphate-group recognition during the transport cycle. Moreover, the hydrophobic pocket that accommodates the lipid tail of S1P and the polar residues involved in binding its headgroup are largely non-conserved between MFSD2B and SPNS2, despite their analogous functional roles (Figure 4D and E).

Previous studies have suggested that S1P transport by HsSPNS2 is only modestly affected by pH and may occur through facilitated diffusion, although another SPNS2 homolog, HnSPNS, has been reported to function as a proton-coupled symporter [12, 13]. We therefore examined whether MFSD2B-mediated S1P export depends on extracellular pH. Transport assays across pH 6.5-8.5 showed only modest changes in activity (Fig. 4F), arguing against strong proton dependence under the tested conditions. Together with its insensitivity to extracellular Na^+ replacement, these results support a facilitated-diffusion model rather than strong Na^+- or proton-coupled transport for MFSD2B-mediated S1P export.

Collectively, our analysis indicates that MFSD2B and SPNS2 follow analogous mechanistic principles for S1P recognition and transport: both contain a hydrophobic pocket for lipid-tail anchoring, positively charged residues positioned to engage the phosphate group, and features consistent with a facilitated-diffusion transport mode. However, the key residues and their spatial arrangements are largely distinct, indicating that MFSD2B

and SPNS2 have evolved different pocket architectures to recognize and transport S1P within the MFS scaffold. These non-conserved pocket architectures provide a structural basis for developing selective S1P transporter inhibitors with reduced cross-reactivity.

S1P-mimic inhibitor cross-activity and development of the TRCS system

Genetic studies have highlighted SPNS2 as a potential therapeutic target in immune and fibrotic diseases. Knockout of *Spns2* in mice confers protection against experimental autoimmune encephalomyelitis (EAE), a widely used preclinical model of multiple sclerosis [14], and *Spns2*-deficient mice are also protected in independent models of renal fibrosis [15]. Accordingly, several SPNS2 inhibitors have been developed [16]. However, many reported SPNS2 inhibitors are S1P-mimic molecules, raising a potential selectivity concern for other S1P transporters such as MFSD2B.

Our structural comparison between MFSD2B and SPNS2 revealed that, although their overall pocket architectures differ substantially, both transporters contain hydrophobic regions capable of accommodating the lipid tail of S1P. Previous structural studies showed that the SPNS2 inhibitor 16d binds at a site that extensively overlaps with the S1P-binding region in the central cavity, consistent with competitive inhibition by blocking substrate access[10]. Notably, three reported SPNS2 inhibitors, 16d, 33p, and 11i, share a similar hydrophobic alkyl tail (Fig. 5A). We

therefore reasoned that these compounds might also inhibit MFSD2B-mediated S1P transport by engaging partially conserved hydrophobic cavity features, thereby causing unintended inhibition of erythrocyte and platelet S1P export.

To test this possibility, we examined the effects of 16d, 33p, and 11i on MFSD2B- and SPNS2-mediated S1P transport. All three compounds inhibited both transporters in a dose-dependent manner, with 33p showing the strongest potency in both cases (Fig. 5B). These data indicate that currently available S1P-like SPNS2 inhibitors display limited selectivity over MFSD2B. Together with the non-conserved pocket features identified above, these results suggest that current S1P-mimic inhibitors may exploit shared substrate-recognition features of MFSD2B and SPNS2, thereby causing cross-activity. Reducing such cross-activity may require the development of new chemical scaffolds that diverge from the S1P-mimic architecture in two ways: replacing the conventional alkyl-like hydrophobic moiety with alternative groups that exploit non-conserved features of the hydrophobic pocket, and redesigning the polar headgroup to engage transporter-specific hydrophilic pockets. Achieving this goal requires high-throughput compound screening, but conventional mass spectrometry (MS)-based S1P quantification is low-throughput and costly, motivating us to develop a more scalable screening approach.

Here we established a transporter-receptor conjugated screening (TRCS) system as an efficient and cost-effective platform for inhibitor screening

(Fig. 5C). In this assay, HEK293T donor cells co-expressing the transporter and sphingosine kinase 1 (SphK1) were supplied with exogenous sphingosine. Intracellular SphK1 converted sphingosine to S1P, which was subsequently secreted into the culture medium in a transporter-dependent manner and captured by albumin [17]. The S1P-containing conditioned medium was then collected and transferred to cells expressing S1P receptors in the presence or absence of test compounds. The S1P level was quantified indirectly through receptor activation, using either Gi-dependent inhibition of cAMP signaling or a β-arrestin-based BRET2 readout [18]. In the BRET2 assay, S1P-containing conditioned medium induced a dose-dependent reporter response, which was strongly suppressed by 33p (Fig. 5D). Thus, TRCS converts transporter-mediated S1P secretion into a receptor-based functional readout, eliminating the need for direct lipid quantification or fluorescent substrate analogs. Compared with conventional assays based on mass spectrometry or NBD-labeled substrates, this platform is less expensive, operationally simple, and readily scalable, providing a practical framework for high-throughput discovery and optimization of selective SPNS2 inhibitors.

Discussion

In this study, we determined a 3.65 Å cryo-EM structure of *Sus scrofa* MFSD2B (SsMFSD2B) in an apo, outward-facing conformation and integrated it with AlphaFold3-based modeling, molecular docking, MD simulations, and mutagenesis to establish a structural framework for S1P

recognition and transport. Comparative analyses with MFSD2A and SPNS2 place MFSD2B in a distinct mechanistic position: MFSD2B is evolutionarily closer to MFSD2A, yet lacks the lysophospholipids-recognition and Na^+-coordination features, while functionally converging with SPNS2 in S1P export through a different pocket architecture. This relationship creates an informative comparison for understanding how MFS lipid transporters achieve substrate selectivity: the translocation scaffold and hydrophobic alkyl-chain anchoring groove are largely conserved, while residues that recognize the hydrophilic headgroup vary in chemical properties and spatial arrangement to accommodate different lipid substrates. Future determination of MFSD2B structures in substrate-bound and additional conformational states will further refine the proposed S1P transport path. More broadly, such studies will help define how conserved MFS scaffolds accommodate chemically diverse lipids through transporter-specific pocket remodeling, providing general principles for understanding lipid transporter selectivity.

In addition, obtaining transporter structures in distinct conformational and ligand-bound states will substantially strengthen structure-guided virtual screening for inhibitor discovery. For alternating-access MFS transporters, different conformations expose different pocket shapes and residue arrangements, which may determine whether molecular docking identifies productive and selective binders. A broader structural ensemble of MFSD2B and SPNS2 would enable more accurate selection of screening

templates, improve docking reliability, and increase the likelihood of identifying true hits with transporter selectivity.

The TRCS system developed here provides a practical platform to further support downstream inhibitor discovery and validation. By converting transporter-mediated S1P secretion into receptor-based functional readouts, TRCS reduces the dependence on low-throughput and costly mass spectrometry-based lipid quantification. This feature should make it useful for large-scale screening and early-stage optimization of S1P transporter inhibitors. Importantly, TRCS is best viewed as a scalable discovery and prioritization platform; promising compounds identified through this approach should be further validated by direct lipid quantification, binding assays, transporter selectivity profiling, and disease-relevant models. Our work may ultimately open new avenues for therapeutic modulation of S1P signaling in metabolic disorders.

Material and methods

S1P release assay in HEK293 cells

HEK293T cells (ATCC CRL-11268; mycoplasma free) were co-transfected with MFSD2B or its mutants together with SphK1 at a ratio of 1.5:0.5 using polyethyleneimine. Next day, transfected cells were harvested and reseeded in 24-well assay plates at a density of 120,000-200,000 cells per well in DMEM with 2% dialyzed FBS and grown to near confluence. Medium was aspirated and 0.4 mL of release buffer (DMEM, 0.2% fatty acid-free BSA, 1 mM 4-deoxypyridinoline, 2 mM NaF, 0.2 mM Na_3VO_4) was added. Sphingosine (5 µM, duplicate wells) was introduced, and plates were incubated for 1 h. Medium was collected and centrifuged; 50 µL supernatant was mixed with 200 µL acetonitrile/methanol/formic acid (80:80:1), held at -80 °C overnight, then centrifuged again. Supernatant (0.1 mL) was transferred to UPLC vials, and S1P were quantified by LC-MS/MS (injection 9 µL).

For pH or cation dependence assays, transfected cells were reseeded in 24-well plates at 3×10^5 cells/well and exposed to different buffers. pH conditions: HBSS pH 7.4; condition 1 (140 mM NaCl, 20 mM MES pH 6.5, 2 mM $CaCl_2$, 1 g/L D-glucose); condition 2 (140 mM NaCl, 20 mM HEPES-NaOH pH 7.5, 2 mM $CaCl_2$, 1 g/L D-glucose); condition 3 (140 mM NaCl, 20 mM Tris-HCl pH 8.5, 2 mM $CaCl_2$, 1 g/L D-glucose). Ionic conditions: condition 1 (HBSS); condition 2 (140 mM NaCl, 20 mM Tris-HCl pH 7.5, 2 mM $CaCl_2$, 1 g/L D-glucose); condition 3 (140 mM

KCl, 20 mM Tris-HCl pH 7.5, 2 mM $CaCl_2$, 1 g/L D-glucose). Growth medium was aspirated and replaced with 0.4 mL/well of the respective buffer containing 1 mM 4-deoxypyridinoline, 2 mM NaF, 0.2 mM Na_3VO_4, and 0.2% fatty acid-free BSA. Sphingosine (5 μM, duplicate wells) was added and incubated for 1 h. Medium was collected and centrifuged; 50 μL supernatant was mixed with 200 μL acetonitrile/methanol/formic acid (80:80:1) and stored at -80 °C overnight. After further centrifugation, 0.1 mL of supernatant was transferred to UPLC vials, and S1P was quantified by LC-MS/MS.

For transporter inhibitors measurement, HEK293T cells were transfected with different plasmids in a six-well plate (SphK1: SPNS2 or MFSD2B = 0.5 μg: 1.5 μg, total plasmid: PEI=2 μg: 8 μg). After 24 h incubation, the medium was removed and supplied with 400 μl DMEM with fatty-acid-free BSA (0.2%), 4-deoxypyridoxine (to 1 mM), NaF (to 2 mM), and Na_3VO_4 (to 0.2 mM) with concentration gradient of inhibitors. After 0.5 h, 5 μM sphingosine was added, and 50 μL medium was mixed with 200 μL extract solution at 1 h.

S1P measurement by LC-MS/MS

S1P in cells and medium was extracted and quantified by LC-MS/MS. The system consisted of a Shimadzu LC coupled to a TripleTOF 6600+ (ABSciex). Separation used a Waters XBridge® Amide HILIC column (3.5 μm, 4.6×100 mm) with gradient elution: mobile phase A (20 mM ammonium acetate, 0.1% ammonium hydroxide, 5 μM ammonium

phosphate in 95:5 water/ACN) and B (ACN). Gradient: 0-2 min, 85% B; 2-3 min, 75% B; 3-7 min, 75% B; 7-8 min, 70% B; 8-9 min, 70% B; 9-10 min, 50% B; 10-12 min, 50% B; 12-12.1 min, 5% B; 12.1-15.5 min, 5% B; 15.5-15.6 min, 85% B; 15.6-21.6 min, 85% B. Injection volume: 5 μL; flow rate: 0.4 mL/min; run time: 21.6 min. ESI parameters: GS1 60, GS2 60, CUR 40, temperature 500 °C, ISVF +5500/-4500 (positive/negative). Data were converted to mzML with MSConvert and processed with EI-MAVEN (v0.12.0) to generate peak tables.

Immunostaining

HEK293T cells (ATCC CRL-11268, mycoplasma-free) were seeded in 6-well plates at 5×10^5 cells/well. The next day, cells were co-transfected with transporter and membrane marker EXOC7-GFP at a 1:1 ratio using polyethylenimine. At 24 h post-transfection, cells were fixed with 4% paraformaldehyde (10 min, RT), permeabilized with 0.2% Triton/0.1% BSA in PBS (10 min, ice), and blocked with 5% BSA in PBS (1 h). Cells were then incubated with anti-Flag M2 monoclonal antibody (1:100, Sigma-Aldrich, F1804) overnight at 4 °C, washed three times with PBS, followed by Alexa Fluor 594 goat anti-mouse IgG secondary antibody (1:200, Thermo Fisher Scientific) for 3 h at 4 °C, washed again three times, stained with DAPI, washed three times, and mounted. Images were acquired with a Zeiss LSM-780 confocal microscope.

Transporter–Receptor Conjugated Screening (TRCS) assay

Donor HEK293T cells co-expressing the transporter and SphK1 were

supplied with sphingosine. Intracellular SphK1 converts sphingosine to S1P, which is secreted into the medium in a transporter-dependent manner and captured by albumin. Conditioned medium is collected, treated with test compounds, and then transferred to reporter cells expressing S1P receptors. Extracellular S1P is quantified indirectly via receptor activation, using either Gi-dependent inhibition of cAMP signaling or a β-arrestin-based BRET2 readout. HEK293T cells co-expressing S1PR1-5 (pcDNA3.1) and a split-luciferase cAMP biosensor (GloSensor, Promega) in 6-well plates. After 48 h, cells were harvested, suspended in HBSS with 10 mM HEPES (pH 7.4) containing 3% D-Luciferin-Sodium-Salt, and seeded into 96-well white clear-bottom plates (15,000 cells/well, 100 µL/well). After 2 h at 37 °C, cells were stimulated with agonist (diluted in assay buffer containing forskolin; initial 40 µM, 1/10 serial dilution) for 30 min at 37 °C. Luminescence was quantified. BRET measured S1PR1-5-mediated G_i protein activation. HEK293T cells were co-transfected with receptor: G_i-Rluc8: G_β: G_γ-GFP2 at 1:1:1:1 ratio using polyethylenimine. After 18 h, cells were replated in opaque white 96-well plates (30,000–50,000 cells/well) in DMEM with 2% dFBS. The next day, medium was removed, and cells were incubated with 40 µL of 7.5 µM coelenterazine 400a (Goldbio) in drug buffer (HBSS, 20 mM HEPES pH 7.4, 0.3% BSA) for 2 min, then treated with 20 µL of serial compound dilutions for 5 min. Plates were read on an LB940 Mithras reader (395 nm and 510 nm filters; 1 s/well). BRET ratio = GFP2 emission (510 nm) /

Rluc8 emission (395 nm); data analyzed with GraphPad Prism 10.0.

This assay is suitable for medium- to high-throughput screening and is compatible with both inhibitor discovery and early-stage structure–activity relationship optimization.

Expression and purification of human MFSD2B

Sus scrofa MFSD2B was cloned into pFastBac vector (Invitrogen) with an N-terminal 10×His tag. Baculovirus was generated using the Bac-to-Bac system (Invitrogen) and used to infect Sf9 cells (Union-Bio) at 2×10^6 cells/mL with 10 mL virus per liter of culture. Cells were harvested after 60 h, frozen in liquid nitrogen, and stored at -80 °C. Cell pellets were disrupted with a Dounce homogenizer (60 cycles on ice) in lysis buffer (25 mM HEPES-Na pH 7.5, 150 mM NaCl, 5% glycerol). After ultracentrifugation (150,000×g, 60 min, 4 °C), the supernatant was discarded and membrane fractions were homogenized in solubilization buffer (same as lysis buffer) with cocktail inhibitors (Sigma). Membranes were dissolved by adding 1% lauryl maltose neopentyl glycol (LMNG) and 0.1% cholesteryl hemisuccinate (CHS) under rotation at 4 °C for 2 h. Debris was pelleted (40,000×g, 30 min, 4 °C), and the supernatant was loaded onto Ni-NTA resin (0.5 mL/L culture). The resin was washed twice with 40 column volumes of wash buffer (25 mM HEPES-Na pH 7.5, 150 mM NaCl, 5% glycerol, 30 mM imidazole pH 8.0, 0.01% LMNG) and eluted with elution buffer (same but 250 mM imidazole). The eluate was subjected to size-exclusion chromatography on a Superdex 200 Increase

10/300 GL column (GE Healthcare) equilibrated with filtration buffer (25 mM HEPES-Na pH 7.5, 150 mM NaCl, 0.005% LMNG, 5 mM DTT). Fractions with the highest MFSD2B concentration were pooled and concentrated for Cryo-EM, S1P was added into the concentrated protein solutions to a final concentration of 100 μM.

Cryo-EM sample preparation and data acquisition

3.5 μL of concentrated SsMFSD2B (5-10 mg/mL) was applied to glow-discharged grids (CryoMatrix M024-Au300-R12/13 or Quantifoil Au 200 1.2/1.3). The grids were blotted for 3.5 seconds and rapidly plunge-frozen in liquid ethane using a Vitrobot (Mark IV, Thermo Fisher Scientific). Single-particle data collection was carried out on a 300 kV Titan Krios G3i transmission electron microscope (Thermo Fisher Scientific), equipped with a Gatan K3 direct electron detector and an energy filter (slit width: 20 eV). Serial EM [19] software was used for data acquisition. Images were collected in super-resolution mode at a magnification of 105,000×, corresponding to a pixel size of 0.425 Å. Each movie was recorded over 50 frames with a total exposure time of 2 seconds. The data were collected in two batches, with electron dose rates of 18.7 and 18.9 e^-/px/s, resulting in total electron doses of 51.76 and 52.32 $e^-/Å^2$, respectively. The defocus range used for imaging was between -1.5 μm and -2.0 μm. A total of 8,644 micrographs were collected.

Data Processing

Multi-frame images were aligned using MotionCor2 [20] by dividing each

image into 25 smaller blocks of 5×5. The aligned images were then imported into cryoSPARC [21] for PatchCTF and CTF estimation. Subsequently, blob picker was used for particle picking and extraction for two-dimensional classification. Using the selected two-dimensional class averages as templates, template picker was applied to perform template-based particle picking. Finally, particles were extracted, yielding 5,390,675, 4,260,346, and 5,421,297 particles, respectively. Multiple rounds of two-dimensional classification were performed, resulting in the selection of 2,735,974 particles. Following this, ab initio reconstruction and two rounds of heterogeneous refinement were conducted, further selecting 920,574 particles. Additional rounds of two-dimensional classification were carried out, narrowing down the dataset to 619,030 particles. Three parallel ab initio reconstructions were then performed, and 207,556 particles were selected. This was followed by five more rounds of ab initio reconstruction, resulting in the selection of 73,714 particles. After one final round of two-dimensional classification, 69,643 particles were subjected to non-uniform and local refinement, leading to a reconstructed density map with a resolution of 3.93 Å. The particles were then re-extracted. A new round of ab initio reconstruction, non-uniform refinement, and local refinement was performed, yielding an improved density map with a resolution of 3.79 Å. Furthermore, the CryoSieve method [22] developed by Hu Mingxu's research group was applied to further sort and select 44,755 high-quality particles. After one final round of ab initio

reconstruction, non-uniform refinement, and local refinement, a final density map with a resolution of 3.65 Å was obtained.

Model building and refinement

The initial structural model was generated using SWISS-MODEL [23] via homology modeling, with the outward-open conformation of MFSD2A (PDB ID: 7OIX) serving as the template. The resulting predicted MsMFSD2B model was then rigidly fitted into the cryo-EM density map in UCSF Chimera and subsequently refined manually in COOT [24]. The complete model was finally refined in Phenix using real-space refinement with secondary structure and geometry restraints [25] and were checked in COOT. Overfitting of the model was checked by refining the model using one of the two independent maps from gold-standard refinement and calculating FSC against both half maps [26]. The final model was validated using Molprobity [27] (Table S1). Structural figures were prepared in UCSF Chimera [28], and UCSF ChimeraX [29].

Molecular docking of S1P

Molecular docking of S1P into the cryo-EM structure of outward-facing SsMFSD2B determined in this study was performed using AutoDock Vina [30]. Prior to docking, the coordinate files for both the receptor and the ligand were prepared using Open Babel 3.1.1 [31] by adding polar hydrogens and converting them into the required PDBQT format. Potential binding sites were identified using the P2Rank algorithm via the PrankWeb server (https://prankweb.cz/), and the geometric center of the top-ranked

pocket (x=122.0, y=124.0, z=126.0) was defined as the center of the docking grid. The grid box dimensions were set to 50×18×18 Å to fully encompass the predicted binding cavity. To ensure a thorough sampling of the conformational space, the exhaustiveness parameter was set to 64. The resulting docking poses were evaluated based on their calculated binding affinities, and the top-ranking pose with the lowest binding energy was selected as the optimal binding mode. All structural visualizations and figures were generated using UCSF ChimeraX (https://www.rbvi.ucsf.edu/chimerax).

AlphaFold 3 Modeling of the SsMFSD2B-S1P

Structural prediction of the SsMFSD2B-S1P complex was performed using a locally deployed instance of AlphaFold 3 [32]. The amino acid sequence of SsMFSD2B (Uniprot ID: F1SCW7) and the chemical representation of S1P (provided as a SMILES string) were utilized as inputs. To ensure comprehensive conformational sampling, the prediction pipeline was executed across 10 independent random seeds, with each seed generating 5 structural models, yielding a total of 50 predicted structures. The resulting models were evaluated and ranked based on their AlphaFold-predicted confidence scores. The five models with the highest confidence scores were selected for downstream analysis. Structural superimposition of these top 5 models revealed a highly convergent binding pose for S1P, indicating a stable and robust predicted interaction mode. All related structural alignments and visualizations were performed using UCSF

ChimeraX and Pymol (https://www.pymol.org/).

Molecular dynamics simulation

The Membrane Builder module in CHARMM-GUI server [33] was used to prepare the simulation inputs, a membrane of pre-equilibrated (310 K) POPC lipids based on the OPM database [34] alignment, TIP3P solvent with 0.15 M Na^+/Cl^- ions and the CHARMM36 force field [35]. The force field of the ligands was generated by the CGenFF program. All MD simulations were performed using GROMACS-2019.4 [36]. The CHARMM36 force-field was used to describe the interactions in the system. Energy minimization was performed for 10000 steps by the steepest descent algorithm and then by the conjugate gradient algorithm. Then a 100 ps NVT simulation was performed at 310 K for solvent equilibration, followed by a 1 ns NPT equilibration to 1 atm using the Berendsen barostat [37]. All MD production simulations were performed with a time-step of 2 fs using Parrinello-Rahman barostat [38]. In all constant temperature simulations, the Bussi (velocity-rescaling) thermostat was used [39]. Long-range electrostatic interactions were treated by the particle-mesh Ewald method [40]. The short-range electrostatic and van der Waals interactions both used a cutoff of 10 Å. All H-bonds were constrained by the LINCS algorithm [41]. For simulations of sodium ion binding, a sodium ion was placed in proximity to the specified two residues D92 and T95 of HsMFSD2B, followed by 100-ns MD simulations performed in triplicate to characterize the binding stability

of the sodium ion.

Statistics and reproducibility

Statistical analyses were performed using GraphPad Prism 10 using an ordinary one-way ANOVA for repeat experiments. All results are expressed as mean ± Standard Error of Mean (SEM) values, n = biological replicates. Differences were considered statistically significant when $p < 0.01$(*); "****" represents $p < 0.0001$.

Acknowledgements

We thank the Kobilka Cryo-EM Center at the Chinese University of Hong Kong, Shenzhen for supporting EM data collection. We thank Cha Wu for assistance with immunostaining. This work was supported by the National Natural Science Foundation of China (grant number 324B2041 to Bin Pang), Postdoctoral Fellowship Program of China Postdoctoral Science Foundation (grant number GZC20251797 to Bin Pang).

Declaration of competing interests

The authors declare no competing interests.

Data availability

Cryo-EM maps and atomic models have been deposited in the Electron Microscopy Data Bank under accession codes: EMD-80802 and in the Protein Data Bank under accession codes: 26PB. All other data supporting this study are available within the article.

Author contributions

R. R. conceived the project and designed all experiments. B. P. conducted all clones, purified protein samples for EM data collection, prepared LC-MS samples and set up TRCS platform. L. Y. prepared the Cryo-EM grids and collected the EM data. B. G. performed the molecular docking and AF3 modeling. Y. H., Z. Q. and W. W. helped to conducted clones and prepared LC-MS samples. R. T. performed the molecular dynamics simulations and computational data analysis. R. H. and L. C. helped to collect samples, operated LC-MS equipment and processed the LC-MC

data. J. W. synthesized all inhibitors. H. J. and H. H. provided the EM data collection and computing support. B. P., B.G., and L. Y. drafted the manuscript. T. X., and R. R. revised the manuscript. All authors analyzed the data and contributed to manuscript preparation.

Reference

1. Ren., R., et al., *A Glimpse of the Structural Biology of the Metabolism of Sphingosine-1-Phosphate.* Contact: The Journal of Inter-Organelle Communication, 2021. **4(2021)**.
2. Pappu, R., et al., *Promotion of Lymphocyte Egress into Blood and Lymph by Distinct Sources of Sphingosine-1-Phosphate.* Science, 2007. **316**(5822): p. 295–298.
3. Kawahara, A., et al., *The Sphingolipid Transporter Spns2 Functions in Migration of Zebrafish Myocardial Precursors.* Science, 2009. **323**(5913): p. 524–527.
4. Vu, T.M., et al., *Mfsd2b is essential for the sphingosine-1-phosphate export in erythrocytes and platelets.* Nature, 2017. **550**(7677): p. 524–528.
5. Fukuhara, S., et al., *The sphingosine-1-phosphate transporter Spns2 expressed on endothelial cells regulates lymphocyte trafficking in mice.* The Journal of Clinical Investigation, 2012. **122**(4): p. 1416–1426.
6. Ghaderi, S. and B. Levkau, *An erythrocyte-centric view on the MFSD2B sphingosine-1-phosphate transporter.* Pharmacology & Therapeutics, 2023. **249**: p. 108483.
7. Yan, N., *Structural Biology of the Major Facilitator Superfamily Transporters.* Annual Review of Biophysics, 2015. **44**(Volume 44, 2015): p. 257–283.
8. Nguyen, L.N., et al., *Mfsd2a is a transporter for the essential omega-3 fatty acid docosahexaenoic acid.* Nature, 2014. **509**(7501): p. 503–506.
9. Nguyen, C., et al., *Lipid flipping in the omega-3 fatty-acid transporter.* Nature Communications, 2023. **14**(1): p. 2571.
10. Pang, B., et al., *Molecular basis of Spns2-facilitated sphingosine-1-phosphate transport.* Cell Research, 2024. **34**(2): p. 173–176.
11. Wood, C.A.P., et al., *Structure and mechanism of blood–brain-barrier lipid transporter MFSD2A.* Nature, 2021. **596**(7872): p. 444–448.
12. Chen, H., et al., *Structural and functional insights into Spns2-mediated transport of sphingosine-1-phosphate.* Cell, 2023. **186**(12): p. 2644–2655.e16.
13. Dastvan, R., et al., *Proton-driven alternating access in a spinster lipid transporter.* Nature Communications, 2022. **13**(1): p. 5161.
14. Donoviel, M.S., et al., *Spinster 2, a sphingosine-1-phosphate transporter, plays a critical role in inflammatory and autoimmune diseases.* The FASEB Journal, 2015. **29**(12): p. 5018–5028.
15. Tanaka, S., et al., *Sphingosine 1-phosphate signaling in perivascular cells enhances inflammation and fibrosis in the kidney.* Science Translational Medicine, 2022. **14**(658): p. eabj2681.
16. Foster, D.J., et al., *Discovery of Potent, Orally Bioavailable Sphingosine-1-Phosphate Transporter (Spns2) Inhibitors.* Journal of Medicinal Chemistry,

2024. **67**(13): p. 11273–11295.

17. Wu, X., et al., *An LC-MS-based workflow measures the export activity of S1P transporters.* Biochemical and Biophysical Research Communications, 2023. **668**: p. 118–124.
18. Yu, L., et al., *Structural insights into subtype-specific agonist recognition by sphingosine-1-phosphate receptors.* PLOS Biology, 2026. **24**(4): p. e3003381.
19. Mastronarde, D.N., *SerialEM: A Program for Automated Tilt Series Acquisition on Tecnai Microscopes Using Prediction of Specimen Position.* Microscopy and Microanalysis, 2003. **9**(S02): p. 1182–1183.
20. Zheng, S.Q., et al., *MotionCor2: anisotropic correction of beam-induced motion for improved cryo-electron microscopy.* Nature Methods, 2017. **14**(4): p. 331–332.
21. Punjani, A., et al., *cryoSPARC: algorithms for rapid unsupervised cryo-EM structure determination.* Nature Methods, 2017. **14**(3): p. 290–296.
22. Zhu, J., et al., *A minority of final stacks yields superior amplitude in single-particle cryo-EM.* Nature Communications, 2023. **14**(1): p. 7822.
23. Bienert, S., et al., *The SWISS-MODEL Repository—new features and functionality.* Nucleic Acids Research, 2017. **45**(D1): p. D313–D319.
24. Emsley, P. and K. Cowtan, *Coot: model-building tools for molecular graphics.* Acta Crystallographica Section D, 2004. **60**(12 Part 1): p. 2126–2132.
25. Adams, P.D., et al., *PHENIX: a comprehensive Python-based system for macromolecular structure solution.* Acta Crystallographica Section D, 2010. **66**(2): p. 213–221.
26. Amunts, A., et al., *Structure of the Yeast Mitochondrial Large Ribosomal Subunit.* Science, 2014. **343**(6178): p. 1485–1489.
27. Chen, V.B., et al., *MolProbity: all-atom structure validation for macromolecular crystallography.* Acta Crystallographica Section D, 2010. **66**(1): p. 12–21.
28. Pettersen, E.F., et al., *UCSF Chimera—A visualization system for exploratory research and analysis.* Journal of Computational Chemistry, 2004. **25**(13): p. 1605–1612.
29. Pettersen, E.F., et al., *UCSF ChimeraX: Structure visualization for researchers, educators, and developers.* Protein Science, 2021. **30**(1): p. 70–82.
30. Eberhardt, J., et al., *AutoDock Vina 1.2.0: New Docking Methods, Expanded Force Field, and Python Bindings.* Journal of Chemical Information and Modeling, 2021. **61**(8): p. 3891–3898.
31. O'Boyle, N.M., et al., *Open Babel: An open chemical toolbox.* Journal of Cheminformatics, 2011. **3**(1): p. 33.
32. Abramson, J., et al., *Accurate structure prediction of biomolecular interactions with AlphaFold 3.* Nature, 2024. **630**(8016): p. 493–500.

33. Jo, S., et al., *CHARMM-GUI: A web-based graphical user interface for CHARMM.* Journal of Computational Chemistry, 2008. **29**(11): p. 1859–1865.
34. Lomize, M.A., et al., *OPM database and PPM web server: resources for positioning of proteins in membranes.* Nucleic Acids Res, 2012. **40**(Database issue): p. D370–6.
35. Huang, J. and A.D. MacKerell Jr, *CHARMM36 all-atom additive protein force field: Validation based on comparison to NMR data.* Journal of Computational Chemistry, 2013. **34**(25): p. 2135–2145.
36. Abraham, M.J., et al., *GROMACS: High performance molecular simulations through multi-level parallelism from laptops to supercomputers.* SoftwareX, 2015. **1-2**: p. 19–25.
37. Berendsen, H.J.C., et al., *Molecular dynamics with coupling to an external bath.* The Journal of Chemical Physics, 1984. **81**(8): p. 3684–3690.
38. Parrinello, M. and A. Rahman, *Crystal Structure and Pair Potentials: A Molecular-Dynamics Study.* Physical Review Letters, 1980. **45**(14): p. 1196–1199.
39. Bussi, G., D. Donadio, and M. Parrinello, *Canonical sampling through velocity rescaling.* The Journal of Chemical Physics, 2007. **126**(1).
40. Darden, T., D. York, and L. Pedersen, *Particle mesh Ewald: An N·log(N) method for Ewald sums in large systems.* The Journal of Chemical Physics, 1993. **98**(12): p. 10089–10092.
41. Applegate DL, B.R., Chvátal V, & Cook WJ, *The Traveling Salesman Problem*, in *Combinatorial Optimization*. 1997. p. 241–271.

Figures and Figure legends

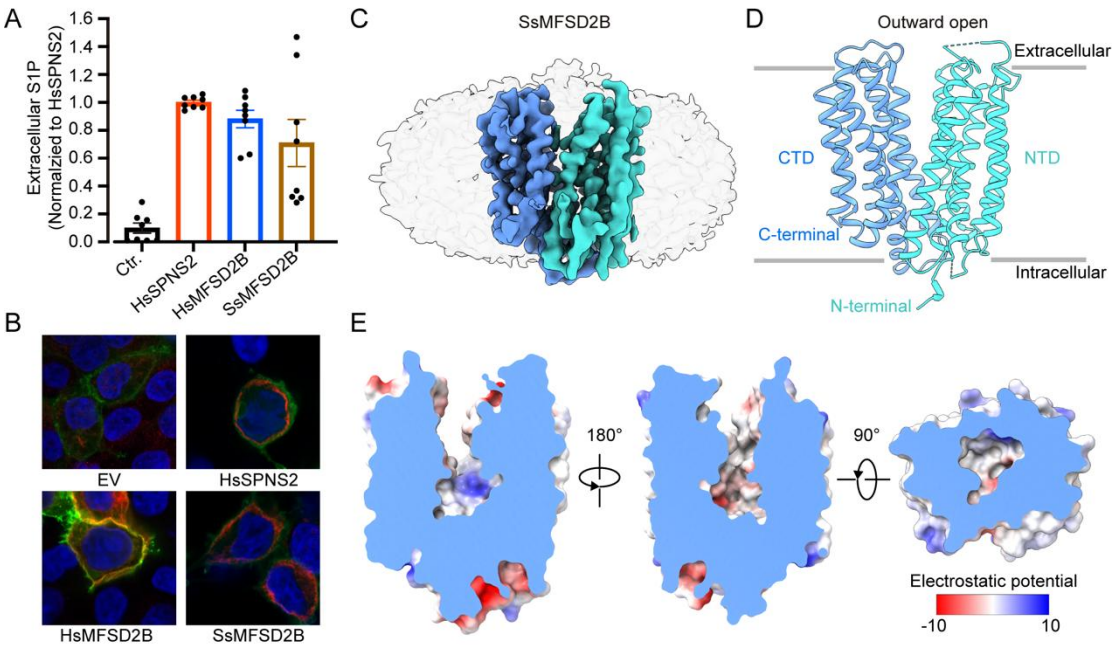

Figure 1. **Functional validation and cryo-EM structure of *Sus scrofa* MFSD2B (SsMFSD2B)**

(A) Transport assay of extracellular S1P level when overexpressing the wild-type form of S1P transporters in HEK293T cells. Data are presented as mean ± SEM. n=4. (B) Immunofluorescence localization of HsSPNS2, HsMFSD2B and SsMFSD2B. Plasma membrane is labeled by GFP (green) fused membrane marker EXOC7. Transporters are labeled by Alexa Fluor 594 (red) goat anti-mouse IgG secondary antibody. Cells were stained with DAPI (blue). (C) Cryo-EM density map of the determined SsMFSD2B structure. Transmembrane helices (TMs) of the C-terminal domain (CTD) and N-terminal domain (NTD) are colored cornflower blue and medium turquoise, respectively. The detergent micelle density is shown in translucent gray. (D) Cartoon representation of the outward-open conformation of SsMFSD2B. TMs of the CTD and NTD are colored as in (C). (E) Central cavity between the CTD and NTD, visualized from multiple cutting angles. The surface and binding pocket are rendered according to electrostatic potential, while the cutting plane is highlighted in blue.

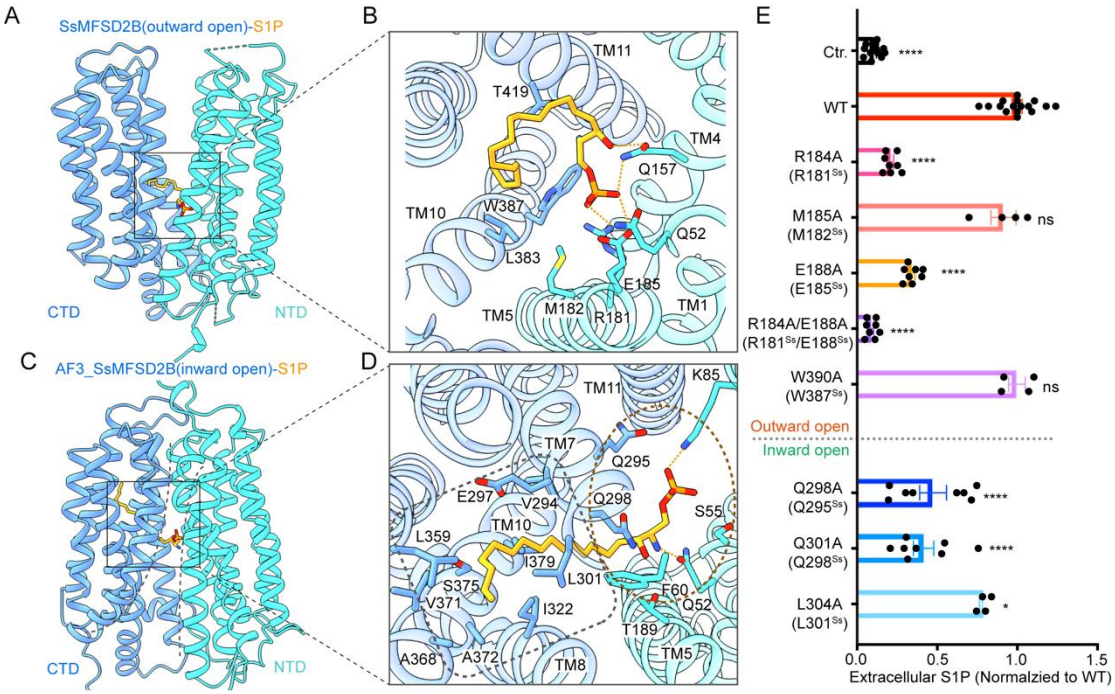

Figure 2. **S1P recognition sites in SsMFSD2B**

(A) Outward-open structure of SsMFSD2B docked with S1P. S1P is depicted as stick models and colored goldenrod. TMs of the CTD and NTD are colored cornflower blue and medium turquoise, respectively. (B) Close-up view of the docked S1P in the outward-open SsMFSD2B binding site. Critical residues and S1P are shown as stick models. Goldenrod dashed lines denote potential hydrogen bonds between S1P and surrounding residues. (C) AlphaFold3-predicted inward-open conformation of SsMFSD2B bound to S1P. S1P and TMs of the CTD and NTD are rendered and colored identically to panel (A). (D) Binding site of S1P in the predicted inward-open SsMFSD2B. Residues and S1P are displayed as stick models. Goldenrod dashed lines indicate putative hydrogen bonds; goldenrod dashed circles highlight a polar environment interacting with the S1P head group. A gray dashed rectangle outlines the hydrophobic pocket accommodating the S1P acyl tail. (E) Transport assay of extracellular S1P level when overexpressing HsMFSD2B wild-type or mutations (R184A, M185A, E188A, R184A-E188A, Q298A, Q301A, L304A, W390A) in HEK293T cells. Data are presented as mean ± SEM. n≧2 biological replicates; $p < 0.0001$(****).

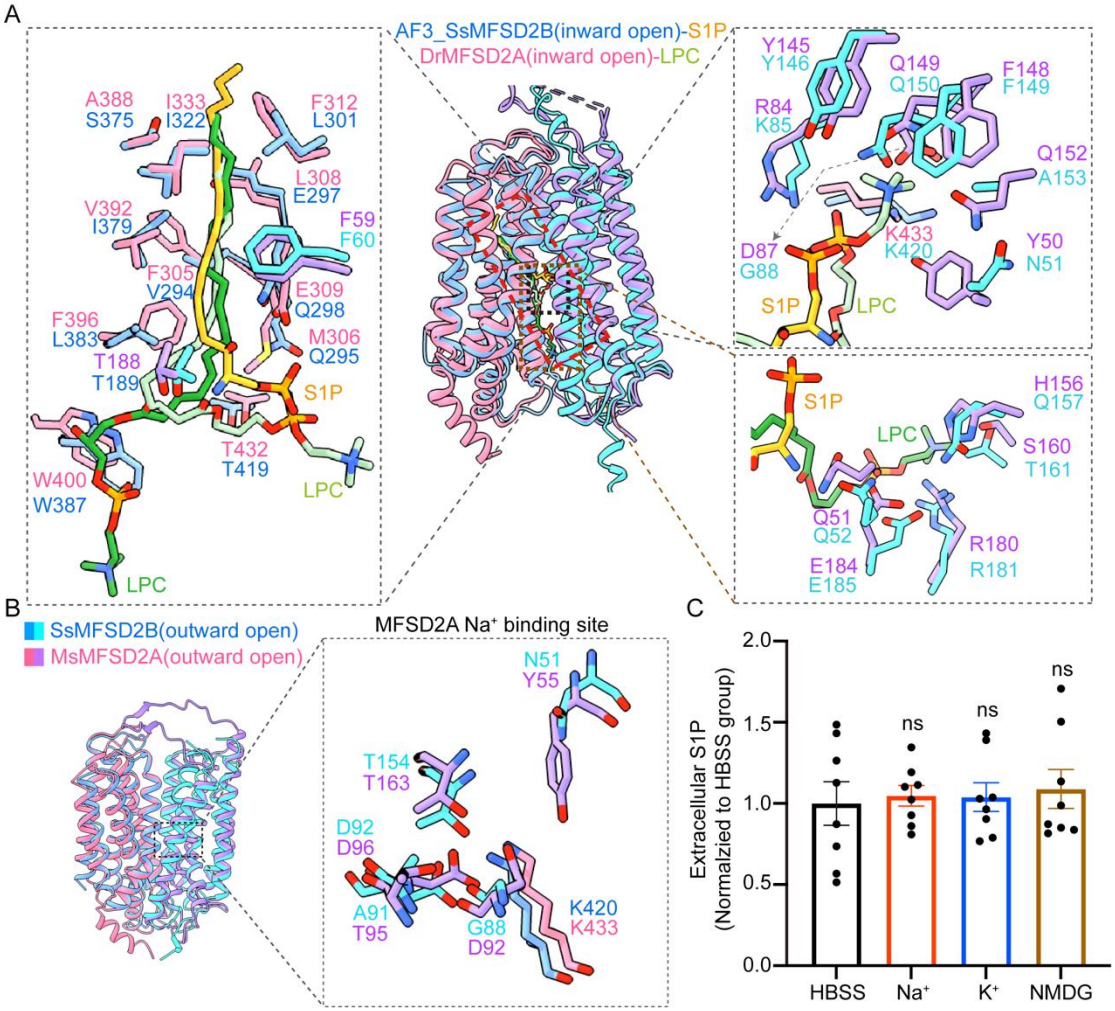

Figure 3. **Structural comparison of SsMFSD2B and MFSD2A**

(A) Superimposed the predicted inward-open structural model of SsMFSD2B with the inward-open structures of DrMFSD2A (PDB IDs: 8D2U and 8D2V). Transmembrane helices (TMs) of the CTD and NTD in SsMFSD2B are colored cornflower blue and medium turquoise, respectively; those in DrMFSD2A are colored pale violet red and medium purple, respectively. S1P in SsMFSD2B and LPC in DrMFSD2A are rendered in goldenrod, dark sea green and forest green, respectively. The left inset provides a close-up view highlighting hydrophobic residues in DrMFSD2A that interact with the alkyl chains of LPC; the corresponding residues in SsMFSD2B are also shown for comparison. The top right inset focuses on polar residues in DrMFSD2A involved in interactions with the head groups of LPC molecules (PDB ID: 8D2U) and the bottom right inset compares with the LPC of PDB ID: 8D2V (colored forest green); the corresponding residues in SsMFSD2B are also shown for comparison. S1P, LPC, and residues are displayed as stick models. (B) Superimposed the outward-open structure

of SsMFSD2B with the outward-open structures of MsMFSD2A (PDB IDs: 7N98). TMs of the CTD and NTD of both SsMFSD2B with MsMFSD2A are colored identically to panel (A). Sodium ion–coordinating residues in MsMFSD2A and their corresponding residues in SsMFSD2B are displayed as stick models in the close-up inset. (C) The transport activity of HsMFSD2B under different ionic environments: HBSS (Hank's balanced salt solution, HBSS); Na^+ (140 mM NaCl, 20 mM Tris-HCl pH 7.5, 2 mM $CaCl_2$, 1 g/L D-glucose); K^+ (140 mM KCl, 20 mM Tris-HCl pH 7.5, 2 mM $CaCl_2$, 1 g/L D-glucose); NMDG (140 mM N-methyl-D-glucamine, 20 mM Tris-HCl pH 7.5, 2 mM $CaCl_2$, 1 g/L D-glucose). Data are represented as mean ± SEM (n = 4 biological replicates).

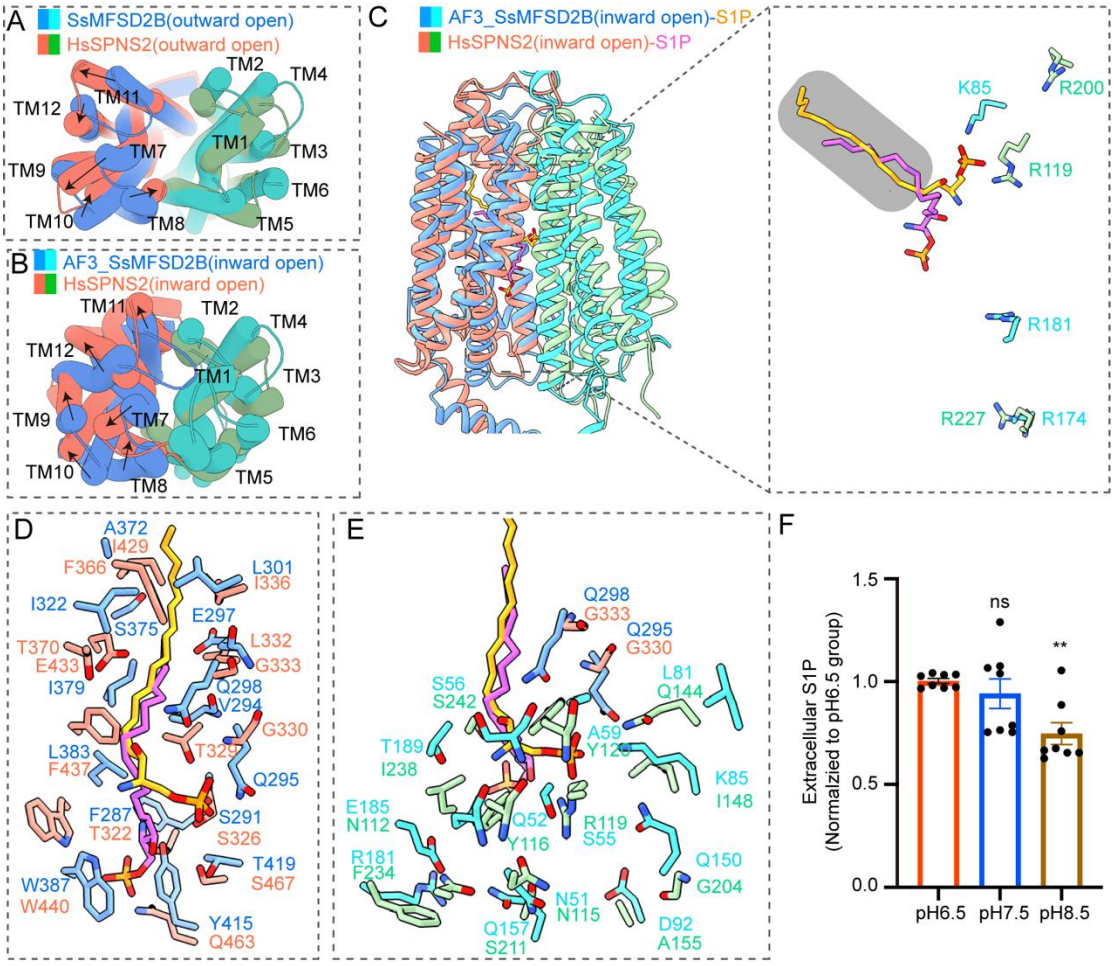

Figure 4. **Structural comparison of SsMFSD2B and HsSPNS2**

(A) Superposition of the outward-open structure of SsMFSD2B with HsSPNS2 (top, PDB ID: 8EX5), and (B) superposition of the predicted inward-open structure model of SsMFSD2B and HsSPNS2 (PDB ID: 8JHQ). Transmembrane helices (TMs) of the CTD and NTD of the SsMFSD2B are colored skyblue and cyan, respectively; those of HsSPNS2 are colored salmon and palegreen, respectively. (B) Superposition of the predicted inward-open structural model of SsMFSD2B and HsSPNS2 (PDB ID: 8JHQ). TMs of the CTD and NTD of both SsMFSD2B with HsSPNS2 are colored identically to panel (A). S1P bound with SsMFSD2B and HsSPNS2A are colored goldenrod and medium orchid, respectively. A close-up view highlights S1P and three positively charged residues (K85, R174, R181 in SsMFSD2B and R119, R220, R227) lining the central cavity of the inward-open conformations of SsMFSD2B with HsSPNS2, shown as sticks. The gray rectangle demarcates a hydrophobic pocket located in the CTD of both transporters. (C) Non-conserved hydrophobic residues forming the hydrophobic pocket in the CTD of SsMFSD2B with HsSPNS2 in panel (B). (D) Non-conserved

polar residues, predominantly located in the CTD, line the central cavity of SsMFSD2B with HsSPNS2 in panel (B). Residues in panel (C) and (D) are shown in as sticks. (E) The transport activity of HsMFSD2B under different pH environments: pH6.5 (140 mM NaCl, 20 mM MES pH 6.5, 2 mM $CaCl_2$, 1 g/L D-glucose); pH7.5 (140 mM NaCl, 20 mM HEPES-NaOH pH 7.5, 2 mM $CaCl_2$, 1 g/L D-glucose); pH8.5 (140 mM NaCl, 20 mM Tris-HCl pH 8.5, 2 mM $CaCl_2$, 1 g/L D-glucose). Data are represented as mean ± SEM (n = 4 biological replicates).

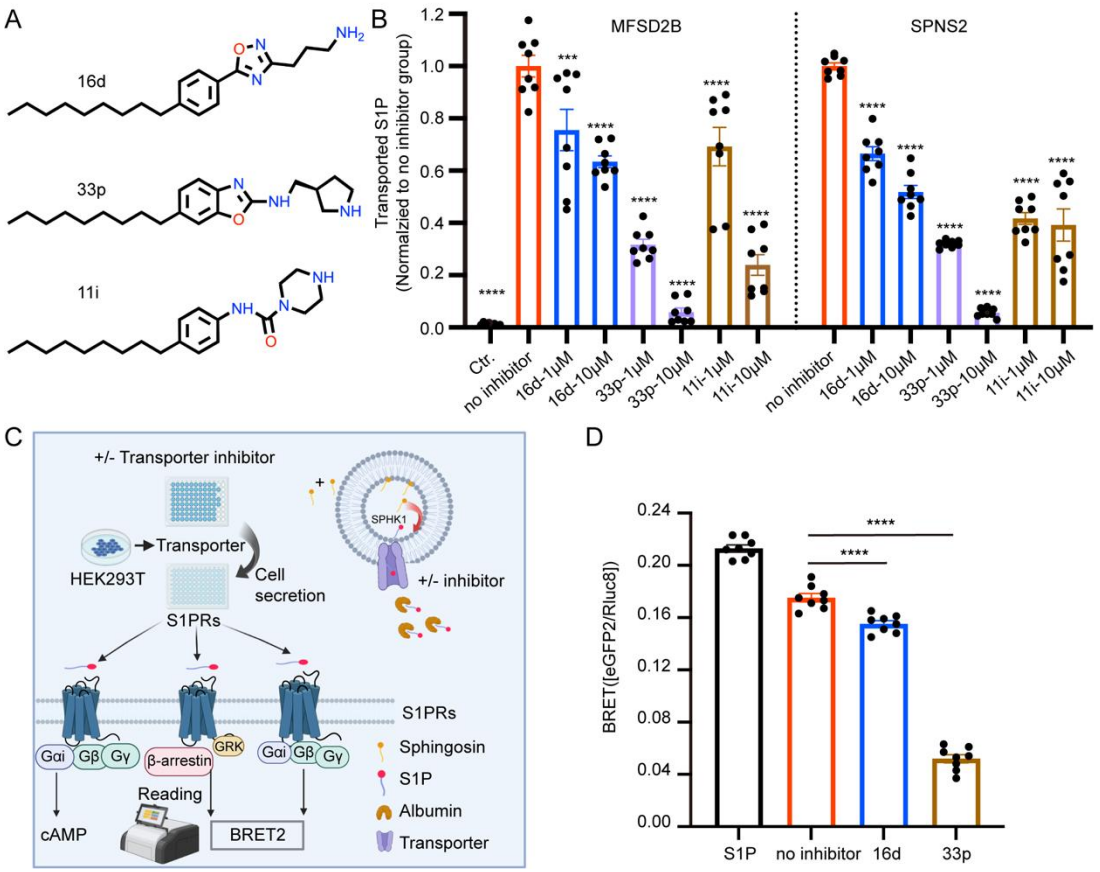

Figure 5. **SPNS2 inhibitor cross-reactivity with MFSD2B and new inhibitors screening system**

(A) Chemical structure of SPNS2 inhibitors 16d, 33p, 11i. (B) Inhibition of S1P release by 16d, 33p, 11i using HEK293T cells overexpressed HsSPNS2 and HsMFSD2B. Data are presented as mean ± SEM. n=4 biological replicates. (C) Schematic overview of the Transporter-Receptor Conjugated Screening (TRCS) assay. HEK293T donor cells co-expressing a S1P transporter and SphK1 are supplied with exogenous sphingosine. Intracellular SphK1 converts sphingosine to S1P, which is then secreted into the culture medium in a transporter-dependent manner and stabilized by albumin. The conditioned medium is collected and transferred to reporter cells expressing S1P receptors. Extracellular S1P is quantified indirectly via receptor activation, using either Gi-dependent cAMP inhibition or a β-arrestin-based BRET2 readout. This platform enables functional screening of transporter inhibitors without the need for direct lipid quantification or fluorescent substrate analogs. (D) BRET2-based detection of transporter-mediated S1P secretion and inhibition. n=4 biological replicates.

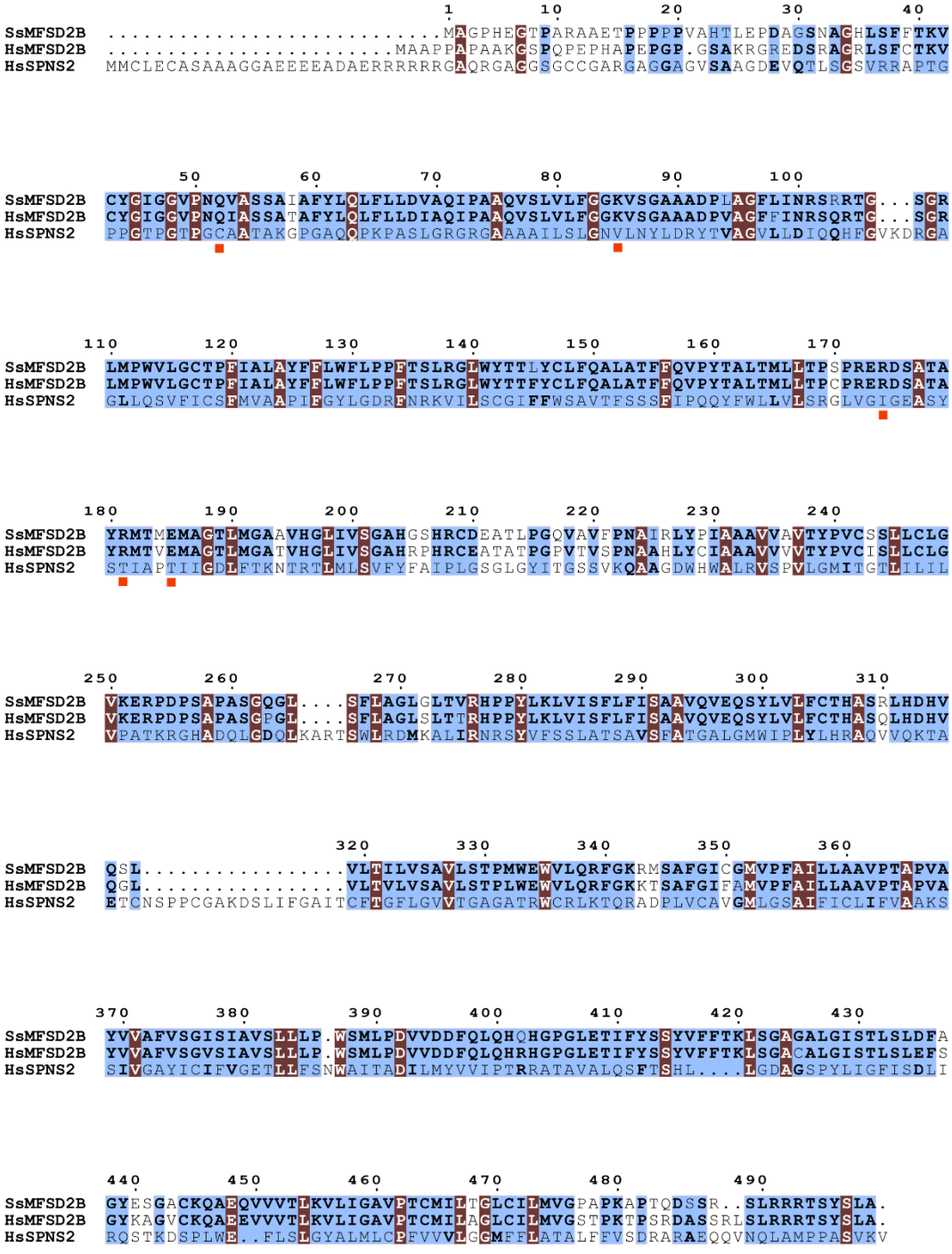

Figure S1. **Sequence alignment of SsMFSD2B, HsMFSD2B, and HsSPNS2**

Sus scrofa MFSD2B: SsMFSD2B; *Homo sapiens* MFSD2B: HsMFSD2B; *Homo sapiens* SPNS2: HsSPNS2

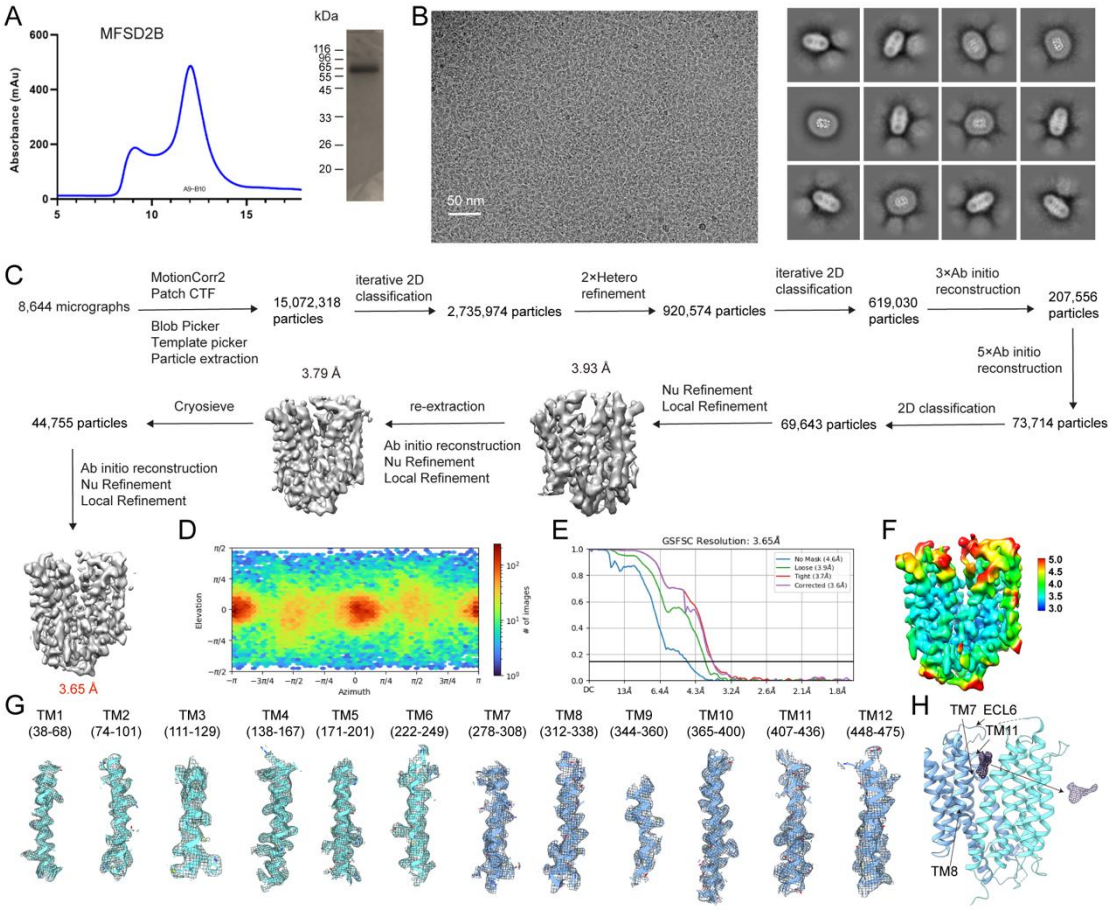

Figure S2. **Purification of SsMFSD2B and structural determination of the outward-open structure of SsMFSD2B**

(A) Gel filtration chromatography elution profile of the purified SsMFSD2B and SDS-PAGE of the eluted protein. (B) Representative micrograph and 2D classes. (C) Flowchart for processing cryo-EM data. (D) Angular distribution of the particles used for the final reconstructions. (E) Fourier shell correlation (FSC) curves of the final refined cryo-EM map are displayed. (F) local resolution of the final map estimated via cryoSPARC. (G) The density maps of the transmembrane and intracellular helices of SsMFSD2B are shown as mesh. (H) Additional density is shown as mesh.

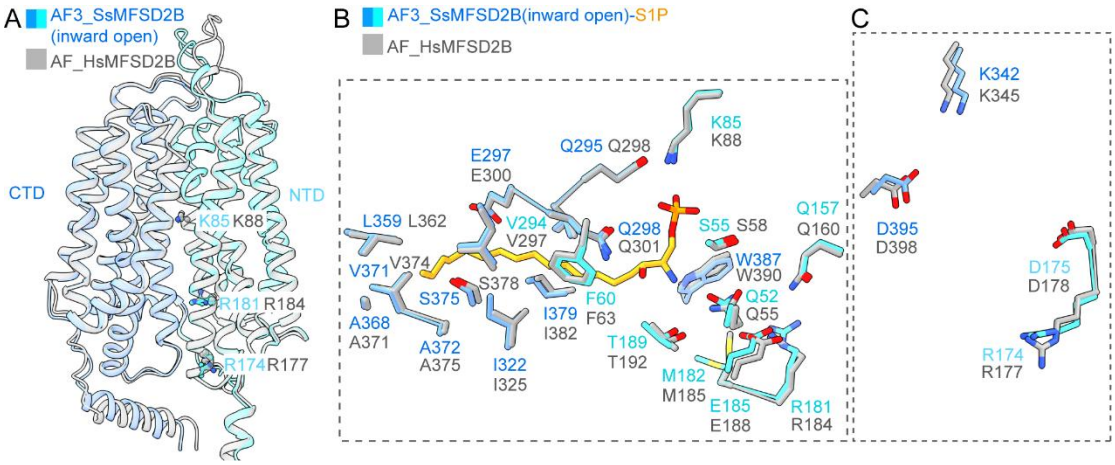

Figure S3. **Highly conserved overall structure and conserved putative substrate-binding sites of SsMFSD2B and HsMFSD2B**

(A) Superposition of Alphafold predicted structural model of SsMFSD2B and HsMFSD2B. TMs of the CTD and NTD in one SsMFSD2B model are colored cornflower blue and medium turquoise, respectively. HsMFSD2B is colored gray. (B) Conserved putative S1P-binding residues of SsMFSD2B and HsMFSD2B. S1P and residues are depicted as stick models. (C) Two interdomain salt bridges pairs shown in Figure S3B are conserved in HsMFSD2B (R177-D398 and D178-K345); Residues are displayed in the predicted inward-open model and shown as stick models.

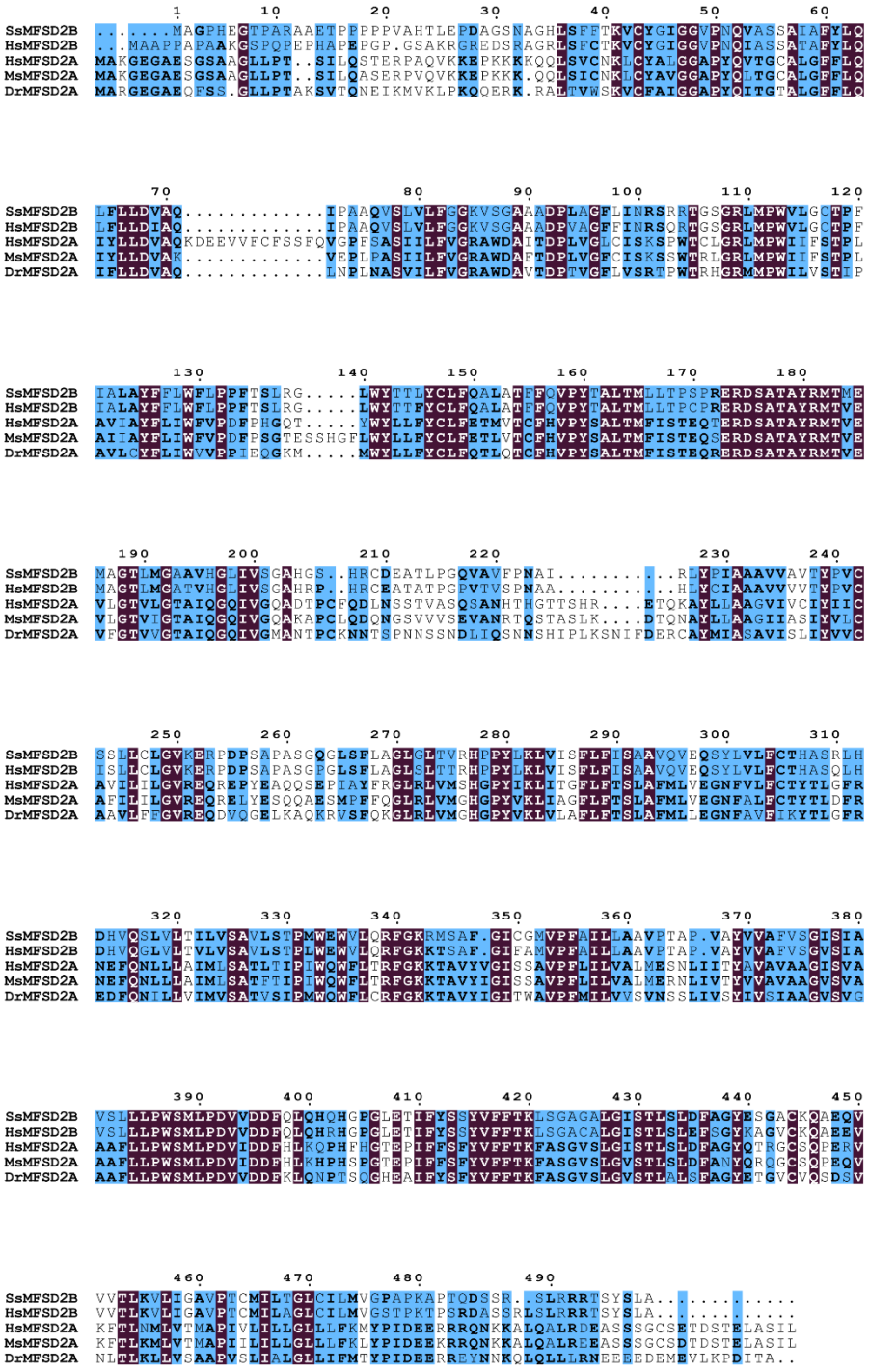

Figure S4. **Sequence alignment of SsMFSD2B, HsMFSD2B, HsMFSD2A, MsMFSD2A, and DrMFSD2A**

Sus scrofa MFSD2B: SsMFSD2B; *Homo sapiens* MFSD2B: HsMFSD2B; *Homo sapiens* MFSD2A: HsMFSD2A; *mouse* MFSD2A: MsMFSD2A; *Danio rerio* MFSD2A: DrMFSD2A.

	SsMFSD2B (EMDB-) (PDB ID:)
Data collection and processing	
Magnification	105,000
Voltage (kV)	300
Electron exposure (e–/Å2)	51.76, 52.32
Defocus range (μm)	-1.5- -2.0
Pixel size (Å)	0.85
Symmetry imposed	C1
Initial particle images (no.)	15,072,318
Final particle images (no.)	44,755
Map resolution (Å)	3.65
FSC threshold	0.143
Map resolution range (Å)	3.0-5.0
Refinement	
Initial model used (PDB code)	7OIX
Model resolution (Å)	3.6/4.0
FSC threshold	0.143/0.5
Model composition	
Non-hydrogen atoms	3126
Protein residues	420
Ligands	1
B factors (Å^2)	
Protein	106.44
Ligand	-
R.m.s. deviations	
Bond lengths (Å)	0.005
Bond angles (°)	1.007
Validation	
MolProbity score	1.93
Clashscore	15.27
Poor rotamers (%)	0.00
Ramachandran plot	
Favored (%)	96.36
Allowed (%)	3.16
Disallowed (%)	0.49

Table S1. **Cryo-EM data collection, refinement and validation statistics**

Video S1
MFSD2B_Na+ bin

Video S1 **Trajectory of molecular dynamic simulations for HsMFSD2B bound with sodium ion**